Online Inertia Estimation of Inverter-Based Resources using Bus Frequency Measurements

Narges Zarean Shahraki, Kaustav Dey, Ting Lin and Aniruddha M. Gole

***Abstract*—The proliferation of converter-based renewable energy sources is expected to cause a significant reduction in the inertial support normally provided by conventional synchronous generators. Although grid-forming control strategies allow for inverters to provide inertia support, the extent of this support depends on the converter ratings and controller parameters, which are often black-boxed by the equipment manufacturers. Therefore, it is important for system operators to assess the available inertia capability of the system. A pragmatic solution proposed in the literature is to estimate the inertia characteristics of such converters using probing signal injections. This approach uses the steady-state deviations in active power and virtual speed due to probing voltage/current injections. However, the virtual speed signal is often an internal variable in a black-boxed controller and not externally available due to proprietary issues. The proposed approach provides a practical solution for evaluating the inertia characteristics of converter-based systems without requiring access to internal variables such as the virtual speed signal. It proposes a new algorithm that obtains a measurement of frequency by passing the measured bus voltage waveform through a Phase-Locked Loop (PLL). Detailed Electro-Magnetic Transient (EMT) simulations are presented to validate the applicability of the proposed approach.**

***Keywords*—Inverter-based Resources (IBRs), Online inertia measurement, Electromagnetic transient (EMT) simulation, Virtual Synchronous Generator, Grid Forming Control.**

I. Introduction

Modern power systems are undergoing rapid transitions towards renewable energy resources, such as wind and solar energy-based generation, to replace conventional synchronous generators. Voltage Sourced Converters (VSC) have become the popular choice for these cases because of their ability to precisely control the power flow in the network. However, the reduction of conventional synchronous generators will reduce the inherent inertia provided by these systems. This is important because the overall inertia is a measure of the ability of the system to resist sudden changes in the system frequency due to generation-load imbalances. To address this issue, grid-forming (GFM) control strategies [1], [2] such as Droop-based GFM [3]–[5] and Virtual Synchronous Generator (VSG) [6]–[9] have been developed to replicate the characteristics of synchronous generators to offer inertia.

Inertia estimation methods can be broadly categorized into four main types: dispatch-based, event-based, ambient-based, and probing-based [10]. Dispatch-based methods [11] utilize Energy Management System data to aggregate the inertia contributions of all dispatched synchronous generators. However, they do not consider the inertia contributions of IBRs, which are becoming an important component in modern grids. Event-driven inertia estimation methods [12]–[14] utilize recorded events from wide-area monitoring systems. The system inertia is estimated based on the knowledge of the event and the initial Rate of Change of Frequency (RoCoF) calculated from measurements [15], [16]. However, accurately estimating RoCoF is complex, requiring signal processing to filter frequency measurements [17], [18]. Additionally, these methods are dependent on the occurrence of major events and their accurate information. Therefore, these methods are not suitable for real-time monitoring of system inertia.

To address these limitations, ambient measurement-based and probing-based inertia estimation methodologies have been proposed in the literature. Ambient measurement-based methods [19], [20] rely on identifying the system model between load changes and frequency variations using the ambient noise behaviour in active power and frequency measurements. The system inertia is then estimated based on the step response of the identified model. However, accurately extracting ambient noise from the measurements is challenging and therefore, affects the accuracy of the estimated inertia. Unlike ambient-based methods, probing-based methods actively inject excitation signals into the system and attempts to identify a linear system model between the probing input and the measured outputs [21], [22]. Data pre-processing techniques, such as filtering and down-sampling, are necessary to refine the measurements. A significant concern is that these methods often require careful design of excitation signals to ensure accurate parameter estimation.

A recently introduced probing-based approach is presented in [23], in which the inertia is estimated from the steady-state active power and virtual speed to determine deviations due to sinusoidal voltage/current injection of a certain frequency. This approach has been tested for the classical model of generators and IBRs emulating classical generator models. To estimate the inertia contribution of grid-forming IBRs, the emulated electrical frequency in the converter controller is used in [23]. A limitation of this approach is its inherent dependence on the converter internal speed signal, which may not be available if the controller has been provided by the manufacturer in a "black-boxed" form, i.e., the internal structure and parameters are not accessible. Although the use of *nearby* synchronously connected generators has been proposed to estimate the virtual speed deviation for grid-following converters, this

N. Z. Shahraki (corresponding author, email: zareansn@myumanitoba.ca), K. Dey (kaustav.dey@umanitoba.ca), T. Lin (lint3456@myumanitoba.ca), and A. M. Gole (aniruddha.gole@umanitoba.ca) are with the Department of Electrical and Computer Engineering, University of Manitoba, Canada.

This work was supported by Mitacs through Mitacs Accelerate program.

Paper submitted to the International Conference on Power Systems Transients (IPST2025) in Guadalajara, Mexico, June 8-12, 2025.

is particularly challenging when the inertia capability of asynchronously connected converters needs to be estimated.

Motivated by these concerns, this paper investigates the applicability of the bus voltage frequency signal as a suitable replacement of the virtual speed signal which is externally accessible and eliminates the need for proprietary internal signals for calculating the inertial characteristics of converter-based systems. This distinction makes our method particularly valuable for black-boxed commercial controllers and asynchronously connected converters. The probing signal injection can be used as an excitation to the system. The inertia of the IBR/synchronous generator under test is then estimated using the measured active power and the bus frequency at its terminals. This scheme alleviates the need to access the converter internal speed signal. The bus frequency can be measured using a Phase Locked Loop (PLL), whose bandwidth must be sufficiently high to capture the steady-state deviations accurately in the frequency range of interest. Using the well-known classical model of synchronous generators, the paper first derives the analytical relationship to understand whether the bus frequency deviations can replicate the behavior of the rotor speed signal accurately. These analytical results are validated using detailed Electro-Magnetic Transient (EMT) simulation studies involving synchronous generators and IBRs endowed with synchronous generator characteristics. The simulation results indicate that the proposed scheme gives accurate results for appropriate injection frequencies.

II. Probing Signal Based Inertia Measurement

The electro-mechanical dynamics of a synchronous generator are characterized by its inertia constant H, which is a measure of the stored kinetic energy in its rotating mass. This stored energy helps to impede frequency changes during disturbances such as sudden changes in power generation or consumption. The electro-mechanical dynamics of the classical model of a synchronous generator can be represented using the well-known "swing" equation, as given in (1).

$$\begin{aligned} \frac{d\delta}{dt} &= (\omega_r - \omega_o) \\ \frac{2H}{\omega_B}\frac{d\omega_r}{dt} + D\,(\omega_r - \omega_o) &= T_m - T_e \end{aligned} \tag{1}$$

where δ and ω_r denote the electrical angle (with respect to a reference axis) and the electrical speed of the rotor, respectively. The variables ω_o and ω_B denote the steady-state electrical frequency of the system (in rad/s) and the base frequency (in rad/s), respectively. T_m and T_e represent the mechanical torque and electrical torque (in per unit), respectively, and D denotes the damping of the machine. Since the synchronous generator frequency is usually very close to the steady-state frequency (i.e. $\omega_r \approx \omega_o$), then T_m and T_e can be substituted by the mechanical power P_m and electrical power P_e of the machine respectively, in per unit.

For small-signal analysis, the system can be linearized about the quiescent operating point. The mechanical power can be assumed to be constant since the associated turbine is much slower compared to the electrical power variations. Therefore, the transfer function between the electrical power deviation $\Delta P_e(s)$ and the speed variation $\Delta\omega_r(s)$ of a synchronous machine is as follows:

$$\frac{\Delta\omega_r(s)}{\Delta P_e(s)} = \frac{-1}{\frac{2H}{\omega_B}s + D} \tag{2}$$

At a certain frequency $s = j\Omega$, the frequency response satisfies the following relationship.

$$\frac{\omega_B\,|\Delta P_e(j\Omega)|}{2\Omega\,|\Delta\omega_r(j\Omega)|} = \left|H + \frac{D\omega_B}{2j\Omega}\right| = H_m \tag{3}$$

Note that (3) refers to the frequency response of the synchronous machine when excited by a modulating signal of frequency Ω. This can be achieved either by injecting a small amplitude modulating voltage V_h or a current signal I_h of frequency $\Omega_h = (\omega_o - \Omega)$, as shown in Fig. 1. The injected voltage and/or current signals are in superposition to the quiescent voltage and/or current sources in the circuit (usually 50/60 Hz) and therefore should be small enough to avoid non-linearities in the response.

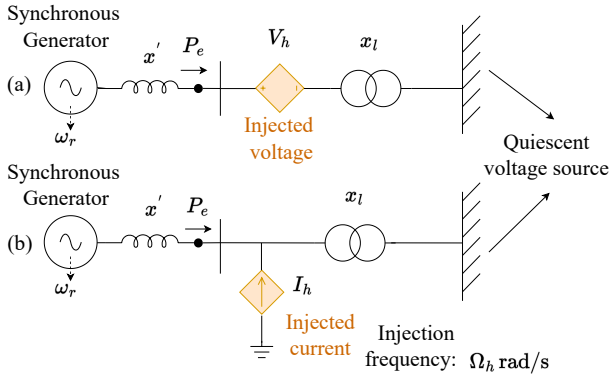

Fig. 1. Probing frequency injection (a) Voltage injection (b) Current injection

For synchronous machines, D is usually very small and therefore, the inertia estimate H_m calculated using (3) gives the inertia constant with reasonable accuracy i.e. $H_m \approx H$. If the damping term D is not negligible, the inertia constant H can be calculated accurately by doing two independent measurements at two different injection frequencies [23]. If the measured inertia is H_{m1} at an injection frequency of f_1 Hz, and the inertia measurement is H_{m2} at injection frequency f_2 Hz, then the inertia H can be calculated as follows [23]:

$$\begin{aligned} H_{m1}^2 = H^2 + \frac{D^2\omega_B^2}{4(2\pi\Delta f_1)^2},\ H_{m2}^2 = H^2 + \frac{D^2\omega_B^2}{4(2\pi\Delta f_2)^2} \\ \implies H = \sqrt{\frac{H_{m1}^2\Delta f_1^2 - H_{m2}^2\Delta f_2^2}{\Delta f_1^2 - \Delta f_2^2}} \end{aligned} \tag{4}$$

where $\Delta f_1 = (f_o - f_1)$ Hz, $\Delta f_2 = (f_o - f_2)$ Hz and $f_o = \frac{\omega_o}{2\pi}$ Hz. In practice, the terminal voltage of the machine is regulated using an automatic voltage regulator [24]. The injection of a probing "voltage" signal at the terminals (point of voltage regulation) of the machine creates an inconsistency, resulting in an erroneous inertia measurement.

Illustrative Example: A 100 MVA, 15 kV synchronous

generator is connected to a 132 kV three-phase ac source through a 15/132 kV transformer, whose parameters and the quiescent operating condition are shown in Fig. 2. To test this probing frequency injection method, the system is simulated at this operating point in an EMT program [25]. The inertia measurement is done using the current injection method, with a current source of magnitude $I_h = 0.05$ kA.

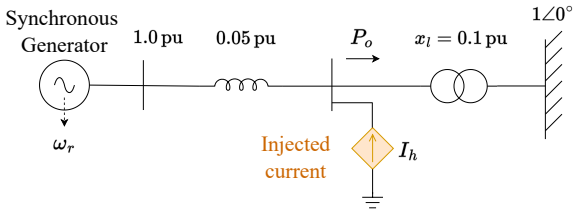

Fig. 2. Schematic for inertia measurement of synchronous generator

The inertia measurement is done for different values of the mechanical damping and for different quiescent operating conditions. To account for the effect of the damping, the inertia is calculated using two different frequencies, as given in (4). These results are reported in Table I along with the combination of injection frequencies.

TABLE I
INERTIA MEASUREMENT FOR CLASSICAL GENERATOR MODEL

		Second injection frequency (Δf_2 in Hz)				
Damping (in pu/rad/s)	Quiescent power (P_o)	0.2 Hz	1	5	10	20
$D = 0.026$	0.1 pu	2.99	2.99	2.99	2.99	3.00
	0.5 pu	2.99	2.99	2.99	2.99	3.00
	0.9 pu	2.99	2.99	2.99	2.99	3.00
$D = 0.053$	0.1 pu	3.00	2.99	2.99	2.99	3.00
	0.5 pu	3.00	2.99	2.99	2.99	3.00
	0.9 pu	3.00	2.99	2.99	2.99	2.99
For all cases, the first injection frequency was $\Delta f_1 = 0.5$ Hz.						

As an illustrative example consider the case with damping D = 0.026 pu/rad/s and active power P_o = 0.9 pu. The injected frequency components are $f_{h1} = 59.5$ Hz and $f_{h2} = 59$ Hz i.e. $\Delta f_1 = 0.5$ Hz and $\Delta f_2 = 1$ Hz. In steady-state, for Δf_1, the amplitudes of the active power deviation is $|\Delta P_{e1}(j\Omega)| = 0.00008$ pu and the rotor speed deviation is $|\Delta\omega_{r1}(j\Omega)| = 0.00141$ rad/s. Similarly, with injection frequency Δf_2 we obtain $|\Delta P_{e2}(j\Omega)| = 0.00041$ pu and $|\Delta\omega_{r2}(j\Omega)| = 0.00395$ rad/s. The inertia values are calculated using (3) as follows.

$$H_{m1} = \frac{\omega_B \times |\Delta P_{e1}(j\Omega)|}{2 \times (2\pi \times \Delta f_1)\,|\Delta\omega_{r1}(j\Omega)|} = 3.39 \text{ s}$$

$$H_{m2} = \frac{\omega_B \times |\Delta P_{e2}(j\Omega)|}{2 \times (2\pi \times \Delta f_2)\,|\Delta\omega_{r2}(j\Omega)|} = 3.10 \text{ s}$$

The inertia constant H is evaluated from these measurements using (4) and is given as follows.

$$H = \sqrt{\frac{H_{m1}^2 \Delta f_1^2 - H_{m2}^2 \Delta f_2^2}{\Delta f_1^2 - \Delta f_2^2}} = 2.99 \text{ s}$$

The inertia measurement approach uses the steady-state variations in the generator rotor speed due to the external injections. However, this necessitates that the inertia of every generator needs to be evaluated separately and the generator rotor speed measurements be available. For grid-forming IBRs emulating classical model characteristics, this approach will require access to the emulated virtual speed. This is particularly challenging since real-life IBR controllers are usually black-boxed by the manufacturers. An alternative signal to the virtual speed can be the bus voltage frequency, which can be directly obtained from the network measurements. The following section investigates the applicability of the bus frequency measurement instead of the virtual speed for inertia estimation.

III. Modelling of Bus Frequency Measurement Scheme for Inertia Estimation

An important aspect that needs to be analyzed is how to measure the bus frequency. One of the ways to measure the frequency of the measured voltage signal is to use a Phase Locked Loop (PLL). However, it is important to understand how the PLL affects the accuracy of the bus frequency measurement, which in turn affects the inertia measurement. For three-phase voltage measurements, the D-Q based PLL is a suitable choice and is analyzed here.

The block diagram of a three-phase D-Q based PLL is shown in Fig. 3. The D-Q transformation in (5) transforms the a-b-c variables to the D-Q-o variables, and $\gamma = \omega_o t + \xi$, ξ being an arbitrary constant.

$$\begin{bmatrix} v_D \\ v_Q \\ v_o \end{bmatrix} = \sqrt{\tfrac{2}{3}} \begin{bmatrix} \cos(\gamma) & \cos(\gamma - \frac{2\pi}{3}) & \cos(\gamma + \frac{2\pi}{3}) \\ \sin(\gamma) & \sin(\gamma - \frac{2\pi}{3}) & \sin(\gamma + \frac{2\pi}{3}) \\ \frac{1}{\sqrt{2}} & \frac{1}{\sqrt{2}} & \frac{1}{\sqrt{2}} \end{bmatrix} \begin{bmatrix} v_a \\ v_b \\ v_c \end{bmatrix} \quad (5)$$

The frequency used in the D-Q transformation ω_o is taken to be the prevailing steady-state frequency so that the D-Q variables are constants in the steady state.

The PLL consists of a low-pass de-noising filter to mitigate noise and other high-frequency components in the voltage measurements and provide a clean reference for the PLL [26]. The filtered D-component is then regulated using a P-I controller, whose output determines the measured frequency ω_m. The following analysis derives the small-signal model of the PLL shown in Fig. 3 to understand the dynamic behavior of the PLL.

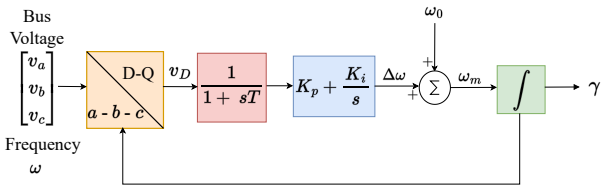

Fig. 3. Schematic of three-phase PLL

Consider the voltages at the PLL input be given as follows.

$$\begin{bmatrix} v_a(t) \\ v_b(t) \\ v_c(t) \end{bmatrix} = \sqrt{\frac{2}{3}} \times V \times \begin{bmatrix} \sin(\omega_o t + \phi) \\ \sin\left(\omega_o t + \phi - \frac{2\pi}{3}\right) \\ \sin\left(\omega_o t + \phi + \frac{2\pi}{3}\right) \end{bmatrix} \quad (6)$$

The D-Q components are generated using the PLL angle γ. At equilibrium, the PLL will lock on to the input voltage waveforms, and therefore the equilibrium value of ω_m will be ω_o. The D-Q voltages can then be written as follows.

$$v_D = V\sin(\phi-\xi),\ v_Q = V\cos(\phi-\xi),\ \gamma = \omega_o t + \xi \quad (7)$$

It is easy to verify that at the equilibrium point, $\xi_o = \phi_o$, where ϕ_o is the equilibrium value of the voltage phase angle. The small-signal model of the PLL at this operating point can then be represented as follows.

$$\frac{d}{dt}\begin{bmatrix}\Delta x_d\\ \Delta x_i\\ \Delta\xi\end{bmatrix} = \begin{bmatrix}-\frac{1}{T} & 0 & -\frac{V_o}{T}\\ 1 & 0 & 0\\ K_p & K_i & 0\end{bmatrix}\begin{bmatrix}\Delta x_d\\ \Delta x_i\\ \Delta\xi\end{bmatrix} + \begin{bmatrix}\frac{V_o}{T} & 0\\ 0 & 0\\ 0 & 0\end{bmatrix}\begin{bmatrix}\Delta\phi\\ \frac{\Delta V}{V_o}\end{bmatrix}$$

The frequency response of the system between the input $\Delta\phi$ and the output $\Delta\xi$ can then be written as follows.

$$\Delta\xi(s) = \frac{(sK_p+K_i)}{s^2(1+sT)+sK_p+K_i}\Delta\phi(s) \quad (8)$$

The frequency $\Delta\omega_m$ and the bus frequency $\Delta\omega$ are related to the PLL output angle ξ and the bus voltage angle ϕ as follows.

$$\Delta\omega_m = \frac{d\Delta\xi}{dt},\ \Delta\omega = \frac{d\Delta\phi}{dt} \quad (9)$$

The overall PLL model between the measured frequency ω_m and the input signal frequency ω can then be obtained by substituting (9) in (8) and can be written as follows.

$$\begin{aligned}\Delta\omega_m(s) &= \frac{(sK_p+K_i)}{s^2(1+sT)+sK_p+K_i}\Delta\omega(s)\\ \implies G_{pll}(s) &= \frac{\Delta\omega_m(s)}{\Delta\omega(s)} = \frac{(sK_p+K_i)}{s^2(1+sT)+sK_p+K_i}\end{aligned} \quad (10)$$

For accurate inertia estimation, the PLL parameters must be carefully chosen so that the frequency response of the PLL is close to $1\angle 0°$ in the injection frequency range.

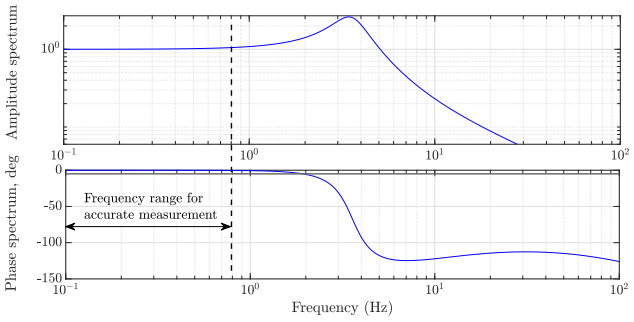

Fig. 4. Frequency response of three-phase PLL parameters

To demonstrate the accuracy of the estimation, the following PLL parameters are chosen: $K_p = 20, K_i = 500$, and $T = 0.001$ s. The frequency response of the PLL, denoted by $G_{pll}(s)$ in (10), is shown in Fig. 4 to determine whether the PLL has sufficient bandwidth to accurately measure the steady-state frequency deviations. Note that the selected PLL parameters are appropriate for measurement up to about 1 Hz, which is sufficient for the proposed scheme.

To verify this, the PLL is connected to a balanced three-phase voltage source of nominal frequency 60 Hz. The source frequency is modulated by a small-amplitude signal, which is given as: $f(t) = 60 + 0.05\times\sin(2\pi\times\Delta f\times t)$ Hz.

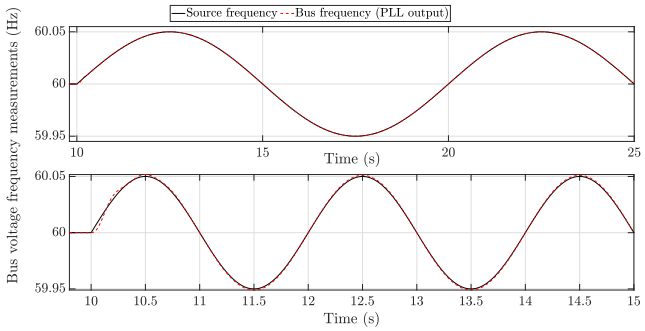

Fig. 5. Steady-state behaviour of PLL frequency measurement

The PLL output along with the source frequency is shown in Fig. 5 for two different modulating frequencies of 0.1 Hz and 0.5 Hz. As expected from the frequency response, these PLL parameters can accurately capture the steady-state perturbations in the input voltage frequency signal. Using this approach, the following section presents the relationship between the bus frequency and the rotor speed of the classical model of a synchronous generator.

IV. Bus Frequency-based Inertia Measurement of Classical Generator Model with Probing Signal

The electro-mechanical dynamics of the classical model of a synchronous generator is shown in Fig. 6. Note that x_g denotes the equivalent impedance of the system, including the generator internal impedance x'_d and the external network impedance x_l. The generator internal voltage E_g is constant

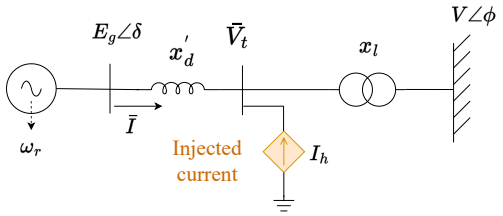

Fig. 6. Schematic of classical generator connected to infinite bus

for the classical model. The electro-mechanical dynamics of the classical generator model are defined as follows.

$$\begin{aligned}\frac{d\delta}{dt} &= (\omega_r-\omega_o)\\ \frac{2H}{\omega_B}\frac{d\omega_r}{dt} + D(\omega_r-\omega_o) &= T_m - (v_D i_D + v_Q i_Q)\\ E_g\angle\delta - jx_g(i_Q+ji_D) &= v_Q + jv_D\end{aligned} \quad (11)$$

Note that H and D denote the inertia constant and the equivalent damping of the generator. The equilibrium values are denoted by the subscript o e.g. ζ_o is the equilibrium value of the variable ζ. Without loss of generality, it is assumed that the equilibrium values of the terminal voltages are $v_{Qo} = V_o$ and $v_{Do} = 0$. This can be arranged by aligning the D-Q transformation angle with the quiescent terminal voltage phase

angle. The dynamical model given in (11) is linearized around the equilibrium point and can be written as follows.

$$\frac{d}{dt}\begin{bmatrix}\Delta\delta\\ \Delta\omega_r\end{bmatrix} = \begin{bmatrix}0 & 1\\ -\frac{V_o E_g\cos(\delta_o)}{Mx_g} & -\frac{D}{M}\end{bmatrix}\begin{bmatrix}\Delta\delta\\ \Delta\omega_r\end{bmatrix} + \frac{V_o E_g}{Mx_g}\begin{bmatrix}0 & 0\\ \cos(\delta_o) & -\sin(\delta_o)\end{bmatrix}\begin{bmatrix}\Delta v_D\\ \Delta v_Q\end{bmatrix} \tag{12}$$

where $M = \frac{2H}{\omega_B}$. The probing signal I_h will cause steady-state perturbations of the injection frequency in the input signals Δv_D and Δv_Q. The D-Q components of the voltage are related to their respective polar components as follows.

$$v_D = V\sin(\phi),\ v_Q = V\cos(\phi) \tag{13}$$

Linearizing, we get

$$\begin{bmatrix}\Delta v_D\\ \Delta v_Q\end{bmatrix} = V_o\begin{bmatrix}\Delta\phi\\ \Delta V_n\end{bmatrix},\ \Delta V_n = \frac{\Delta V}{V_o}, \Delta\theta = \int \Delta\omega\, dt \tag{14}$$

where $\Delta\omega$ denotes the bus frequency deviation. Applying Laplace transform in (12) and substituting (14), we get

$$\Delta\omega_r(s) = \underbrace{\frac{V_o E_g\cos(\delta_o)}{Mx_g s^2 + Dx_g s + V_o E_g\cos(\delta_o)}}_{A(s)}\Delta\omega(s) - \frac{V_o E_g\sin(\delta_o)}{Mx_g s^2 + Dx_g s + V_o E_g\cos(\delta_o)}\Delta V_n(s) \tag{15}$$

The deviation in bus frequency $\Delta\omega$ is related to the rotor speed deviation $\Delta\omega_r$ through the transfer function $A(s)$. Note that if the internal reactance of the model were small, i.e., $x_g \approx 0$, then $A(s) = 1$, indicating that the terminal voltage frequency deviation would be a good approximation of the rotor speed deviation. This substitution ensures that our proposed method remains robust even when direct rotor speed measurements are unavailable. This is illustrated with the following numerical case study.

A. Numerical Case Study

Consider a synchronous generator connected to an infinite bus through an external impedance, as given in (11). The equilibrium values of the terminal voltage V_o and the internal voltage E_g are both 1 pu. The steady-state frequency f_o is 60 Hz and the classical model parameters are $H = 3$ s and $D = 0.5$ pu/rad/s. The transformer leakage reactance is $x_l = 0.1$ pu and the generator is injecting 0.8 pu active power into the network. The frequency response of $A(s)$ is plotted in Fig. 7 for different values of x'_d. Note that the frequency response of the transfer function $A(s)$ is approximately $1\angle 0°$ for frequencies less than 0.4 Hz for both values of x'_d. However, at higher frequencies, the deviation is much larger for higher x'_d, indicating that the rotor speed deviations may not be accurately captured in the bus frequency measurements. The bandwidth of the PLL and the frequency range of the injected signal should therefore cover the frequencies over which $A(s) \approx 1$.

To validate this, the classical model-based system is simulated in an EMT platform and the system is probed with a current injection as shown in Fig. 1 using the approach described in Section II. The PLL parameters selected here are as follows: $K_p = 20, K_i = 500, T = 0.001$ s. The injection frequency is $\Delta f = 0.3$ Hz, and the steady-state waveforms of the generator terminal voltage frequency ω and the rotor speed ω_r are shown in Fig. 8 for different values of x'_d. As expected, the mismatch is quite significant when x'_d is higher, which will cause the inertia estimation to be inaccurate. To overcome this limitation, a compensation strategy for the internal impedance is proposed, which is now explained.

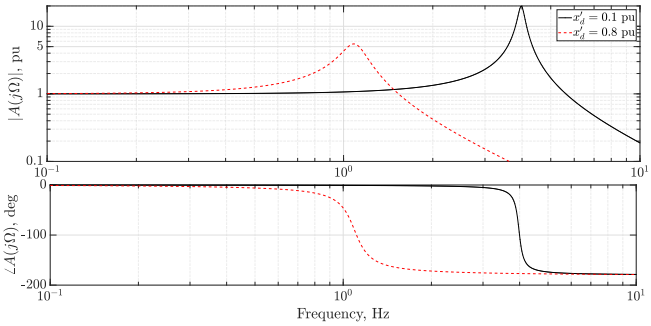

Fig. 7. Frequency response of $A(s)$ for different values of x'_d

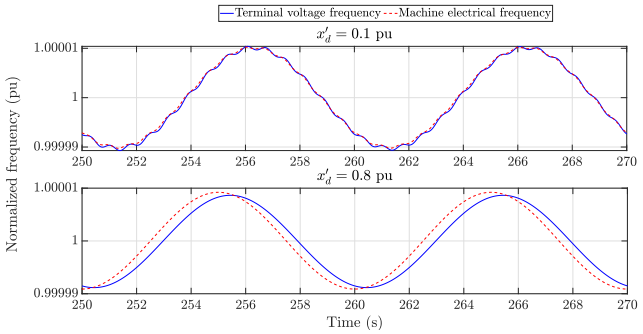

Fig. 8. Comparison of terminal voltage frequency and rotor speed waveforms for classical synchronous machine model

B. Internal Impedance Compensation

Since the phase angle of the internal voltage δ of the classical model relates to the rotor angle, it is expected that the electrical frequency of the internal voltage E_g can accurately capture the behavior of the rotor speed signal ω_r. Although the internal voltage is not measurable, the internal voltage can be calculated using the terminal voltage and current measurements, as given in (16).

$$E_{gQ} + jE_{gD} = v_{tQ} + jv_{tD} + jx'_d(i_Q + ji_D) \tag{16}$$

The D-Q components of the voltages and currents are calculated using the D-Q-o transformation given in (5). The D-Q components of the internal voltage are then converted back to the phase variables and are given as inputs to the PLL, as illustrated in Fig. 9. The frequency of this signal (measured using a PLL) is then used for inertia measurement, as described in Section II. To ensure that the internal voltage E_g is obtained appropriately w.r.t. the terminal voltage, the D-Q transformations are done with the same transformation angle γ as shown in Fig. 9. The frequency of the transformation is

taken to be the steady-state frequency i.e. 60 Hz. The accuracy of this approach is verified with the following case study.

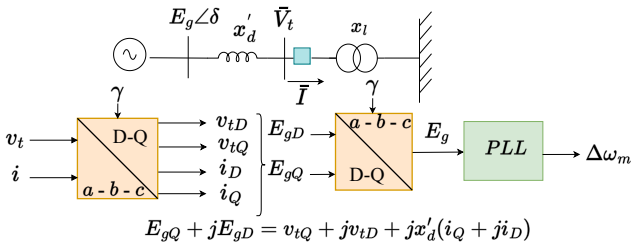

Fig. 9. Schematic of internal voltage measurement approach

The inertia estimation is done with and without compensating for the internal impedance of the generator with $x_d' = 0.8$ pu. As described earlier, the inertia is measured using two different injection frequencies. The measured inertia values for different injection frequencies are reported in Table II. As expected, there is a significant error in the inertia measurement at higher loading levels when the internal impedance compensation is not done. However, with the compensation, the inertia estimation is quite accurate.

TABLE II
INERTIA MEASUREMENT FOR CLASSICAL GENERATOR MODEL

Compensation included?	Quiescent power (P_o)	Injection frequency (Δf_2 in Hz) 0.1	0.25	0.3	0.4	0.5
Yes	0.1 pu	2.99	2.96	2.96	2.94	2.92
	0.5 pu	2.99	2.96	2.96	2.94	2.92
	0.9 pu	2.98	2.96	2.96	2.94	2.92
No	0.1 pu	3.1	3.14	3.16	3.22	3.29
	0.5 pu	3.14	3.17	3.21	3.27	3.35
	0.9 pu	3.32	3.39	3.41	3.47	3.56
For all cases, the first injection frequency was $\Delta f_1 = 0.2$ Hz						

The results presented in this section are useful to understand the behaviour of the classical model of synchronous generators and, therefore, also for inverters emulating such characteristics. The following section presents the inertia estimation of grid-forming inverters emulating classical synchronous generator models, commonly referred to as "Virtual Synchronous Generators" (VSG).

V. Inertia Measurement of Grid-Forming Inverters with VSG Control

The higher bandwidth of power-electronic converters allows to emulate the dynamics of conventional synchronous machines, also known as the VSG control strategy. The control structure of a VSG is illustrated in Fig. 10. The swing equation in (1) is implemented in the power synchronization loop. The emulated angle θ is used as the reference angle for the voltage and current control loops of the VSC inverter. In addition to these components, the controller also includes overcurrent limiters to prevent excessive fault currents.

The schematic of the power circuit of a two-level VSC with VSG-based control is shown in Fig. 11. The inverter is connected to an LCL filter to filter out the switching

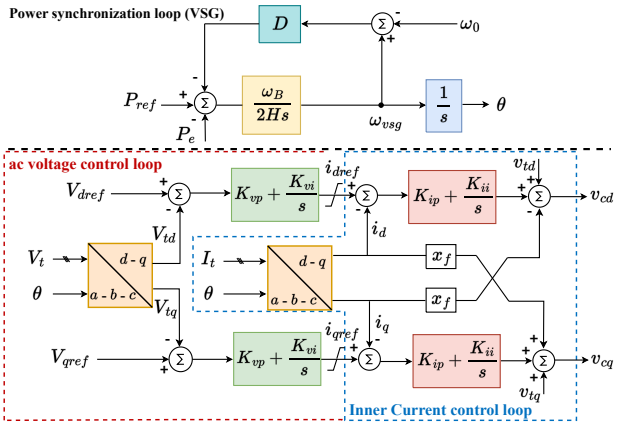

Fig. 10. VSG control structure

frequency components. The converter is interfaced to the external ac system through a step-up transformer at the Point Of Interconnection (POI), as shown in the figure. The voltage and current measurements V_t and I_t, respectively, are used by the controller to generate the switching pulses.

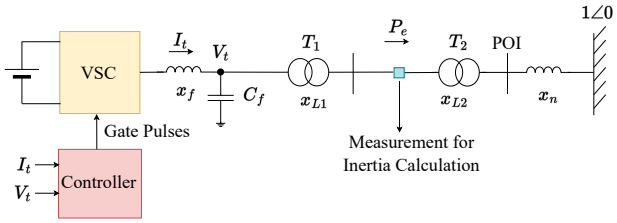

Fig. 11. Power circuit schematic of VSC-based inverter

The inertia measurement approach described in Section II is utilized to measure the inertia capability of VSG-based converters in [23]. The steady-state deviations in the measured active power P_o and the frequency of the internal voltage is used instead of the converter speed signal ω_{vsg} to estimate the emulated inertia H. Although the VSG could have different parameters from the real synchronous generator, their structures and transfer functions are the same. Therefore, the treatment used for the classical generator models in the previous section can directly be extended to the VSG case.

The proposed approach uses the fundamental relationship between power and frequency to estimate inertia and applies to any control mode or type of converter e.g., GFM, Grid Following (GFL), etc. Any control method that changes the power order as a function of frequency affects the virtual inertia and can be detected by this method. Since the approach is based on steady-state measurements, the inertia estimation is not expected to be influenced by over-current limiting strategies such as virtual impedance compensation [27], [28], which is primarily active during short-circuit faults and overload conditions. Although experimental results are presented here for specific control modes, the proposed method is versatile and can be applied to other control modes as well.

Since the converter control regulates the low voltage side

of the transformer V_t, this voltage is analogous to that of the internal voltage E_g of a classical synchronous machine. Therefore, the frequency of this "internal" voltage can serve as a better representative of the converter speed signal ω_{vsg}. As a straightforward extension of the approach presented in the previous section, this internal voltage can either be directly measured or can be obtained using the compensation approach presented earlier. The frequency of this internal voltage can be measured using the PLL, which is used for the inertia measurement. The accuracy of this approach is now presented using a numerical case study.

Case Study: A two-level 200 MVA, 230 kV VSG is considered here. The circuit parameters of the VSG along with the controller parameters are given in Table III. The VSC converter is connected to a 230 kV ac system. The emulated inertia constant and damping are $H = 3$ s and $D = 0.05$ pu/(rad/s), respectively. For the inertia estimation, a probing current signal of magnitude 0.02 kA is applied at the POI. The inertia is first calculated for different quiescent operating conditions using the virtual speed signal ω_{vsg} and is given in Table IV. Since $D \neq 0$, the inertia is calculated using two injection frequencies as explained in Section II. As expected, the converter virtual speed signal provides a very accurate estimate of the emulated inertia constant.

TABLE III
VSG CONVERTER SYSTEM PARAMETERS

Converter reactance (x_f)	0.335 mH
Filter capacitance (C_f)	700 μF
Converter transformer T_1 winding voltage	0.69/13.8 kV
Converter transformer T_1 leakage reactance (x_{L1})	0.0375 pu
Converter transformer T_1 rating	200 MVA
POI transformer winding voltage	13.8/230 kV
POI transformer T_2 rating	200 MVA
POI transformer T_2 leakage reactance (x_{L2})	0.125 pu
Network reactance (x_n)	0.014 pu
DC link voltage	1.45 kV
Voltage loop controller gains (K_{vp}, K_{vi})	(10,10)
Current loop controller gains (K_{ip}, K_{ii})	(0.5,100)

TABLE IV
INERTIA MEASUREMENT OF VSG CONVERTER WITH ω_{vsg} SIGNAL

		Second injection frequency (Δf_2 Hz)				
Damping (in pu/rad/s)	Quiescent apparent power $(P_o + jQ_o)$	0.3	0.4	0.6	0.7	0.8
$D = 0.05$	0.1 pu	3.03	3.02	3.01	3.00	3.00
	0.5 pu	3.02	2.99	2.96	2.96	2.95
	0.9 pu	2.88	2.88	2.87	2.88	2.88
	$(0.25 + j0.5)$ pu	3.04	3.02	3.00	2.99	2.98
	$(0.7 + j0.25)$ pu	2.97	2.95	2.93	2.93	2.92
For all cases, the first injection frequency was $\Delta f_1 = 0.5$ Hz.						

To evaluate the accuracy of the bus frequency-based approach, the bus voltage and current are measured, as shown in Fig. 11. The frequency of the terminal voltage are measured by the PLL and is used for inertia measurement (without internal impedance compensation). The PLL parameters are: $K_p = 10, K_i = 500, T_f = 0.001$ s. The calculated inertia values for different operating scenarios are shown in Table V. The steady-state deviations in the internal voltage are then calculated by compensating for the impedance x_{L1}. The frequency of this signal is then measured using the same PLL. The estimated inertia (for same D and H values) with the PLL-based frequency measurements (along with the relative errors) are presented in Table VI for the same operating conditions. Comparing the results of Tables V and VI, the internal impedance compensation improves the inertia estimate, as was indicated in Section IV. An interesting observation is that the inertia estimate is more accurate when the VSC operates at a higher power injection level. The accuracy of the measured inertia is acceptable when the injection frequency is up to about 1 Hz, which is within the bandwidth of the PLL.

TABLE V
INERTIA MEASUREMENT OF VSG CONVERTER WITH BUS FREQUENCY (WITHOUT INTERNAL IMPEDANCE COMPENSATION)

		Quiescent power injection $(P_o + jQ_o)$ pu				
Injection (Δf_2 Hz)		$(0.1+ j0)$	$(0.5+ j0)$	$(0.9+ j0)$	$(0.25+ j0.5$	$(0.7+ j0.25)$
0.3	Inertia (s)	3.49	3.3	2.82	3.42	3.14
	Error (%)	16.3	10	6	14	4.66
0.4	Inertia (s)	3.47	3.27	3.0	3.4	3.14
	Error (%)	15.7	9	0	13.3	5
0.6	Inertia (s)	3.48	3.27	3.04	3.4	3.15
	Error (%)	16	9	1.33	13.3	5
0.7	Inertia (s)	3.48	3.28	3.05	3.41	3.19
	Error (%)	16	9.33	1.66	13.6	6.33
0.8	Inertia (s)	3.29	3.29	3.07	3.42	3.2
	Error (%)	9.66	9.66	2.33	14	6.66
For all cases, the first injection frequency was $\Delta f_1 = 0.5$ Hz						

TABLE VI
INERTIA MEASUREMENT OF VSG CONVERTER WITH BUS FREQUENCY (WITH INTERNAL IMPEDANCE COMPENSATION)

		Quiescent power injection $(P_o + jQ_o)$ pu				
Injection (Δf_2 Hz)		$(0.1+ j0)$	$(0.5+ j0)$	$(0.9+ j0)$	$(0.25+ j0.5$	$(0.7+ j0.25)$
0.3	Inertia (s)	3.33	3.15	2.84	3.27	3.02
	Error (%)	11	5	5.33	9	0.66
0.4	Inertia (s)	3.29	3.12	2.86	3.23	3.00
	Error (%)	9.66	4	4.66	7.66	0
0.6	Inertia (s)	3.24	3.07	2.85	3.18	2.97
	Error (%)	8	2.33	5	6	1
0.7	Inertia (s)	3.21	3.04	2.85	3.15	2.94
	Error (%)	7	1.33	5	5	2
0.8	Inertia (s)	3.18	3.01	2.81	3.12	2.92
	Error (%)	6	0.33	6.33	4	2.66
For all cases, the first injection frequency was $\Delta f_1 = 0.5$ Hz						

Effect of variation in operating conditions: To verify the accuracy of the inertia estimation during change in operating condition, the active power reference of the GFM converter of the test system is increased. Fig. 12 illustrates this point by considering the case where a power order change from 0.1 to 0.2 pu is applied at $t = 7.1$ s as shown by Fig. 12 (a). The injected power follows the reference input and the steady-state power waveform has an oscillatory component, whose frequency is same as that of the injection frequency for inertia measurement. After a short period (approximately 4 s), the estimated inertia value stabilizes and converges to its pre-disturbance value, as shown in Fig. 12 (b).

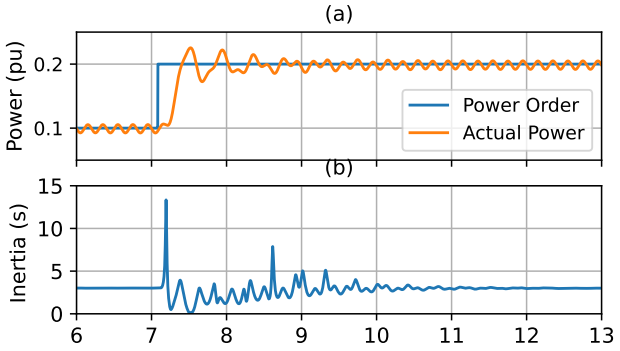

Fig. 12. Effect of active power Change on inertia estimation

VI. Conclusions

This paper presents a probing-based inertia measurement approach using the bus frequency signal for grid-forming inverters emulating virtual synchronous generator characteristics. The frequency of the internal voltage provides an accurate estimation of the virtual speed, thereby improving the accuracy of the inertia measurement. The steady-state deviations in the bus frequency signal are utilized to calculate the emulated inertia of these inverters. A major advantage of the proposed approach is that it can be applied even when only black-boxed models of the IBR are available. Although earlier approaches utilizing controller signals can provide very accurate inertia measurement ($< 3\%$ error), they rely on the availability of controller internal signals. The proposed approach also provides reasonably accurate inertia estimation ($< 5\%$ error except for very low loading conditions). This validates the practicality of our approach, particularly in cases where proprietary constraints prevent access to converter internal signals. EMT-based numerical case studies are presented to validate the accuracy of the proposed approach.

References

[1] E. S. I. Group, "Grid-forming technology in energy systems integration," tech. rep., ESIG, 2022.

[2] N. I.-B. R. P. W. G. I. report, "Grid forming technology: Bulk power system reliability consideration," tech. rep., NERC, 2021.

[3] A. Engler, "Device for Parallel Operation of Equal Range Single-Phase or Three-Phase Voltage Sources," *EP1286444B1*, 2001.

[4] W. Du, Z. Chen, K. P. Schneider, R. H. Lasseter, S. P. Nandanoori, F. K. Tuffner, and S. Kundu, "A comparative study of two widely used grid-forming droop controls on microgrid small-signal stability," *IEEE Journal of Emerging and Selected Topics in Power Electronics*, vol. 8, no. 2, pp. 963–975, 2019.

[5] R. H. Lasseter, Z. Chen, and D. Pattabiraman, "Grid-forming inverters: A critical asset for the power grid," *IEEE Journal of Emerging and Selected Topics in Power Electronics*, vol. 8, no. 2, pp. 925–935, 2019.

[6] Q. C. Zhong and G. Weiss, "Synchronverters: Inverters that mimic synchronous generators," *IEEE transactions on industrial electronics*, vol. 58, no. 4, pp. 1259–1267, 2010.

[7] M. Chen, D. Zhou, and F. Blaabjerg, "Modelling, implementation, and assessment of virtual synchronous generator in power systems," *Journal of Modern Power Systems and Clean Energy*, vol. 8, no. 3, pp. 399–411, 2020.

[8] K. I. Sakimoto, K. Sugimoto, and Y. Shindo, "Low voltage ride through capability of a grid connected inverter based on the virtual synchronous generator," in *2013 IEEE 10th International Conference on Power Electronics and Drive Systems (PEDS)*, pp. 1066–1071, IEEE, 2013.

[9] J. Alipoor, Y. Miura, and T. Ise, "Power system stabilization using virtual synchronous generator with alternating moment of inertia," *IEEE journal of Emerging and selected topics in power electronics*, vol. 3, no. 2, pp. 451–458, 2014.

[10] K. Prabhakar, S. K. Jain, and P. K. Padhy, "Inertia estimation in modern power system: A comprehensive review," *Electric Power Systems Research*, vol. 211, 2022.

[11] Y. Bian, H. Wyman-Pain, F. Li, R. Bhakar, *et al.*, "Demand side contributions for system inertia in the GB power system," *IEEE Transactions on Power Systems*, vol. 33, no. 4, pp. 3521–3530, 2017.

[12] D. P. Chassin, Z. Huang, M. K. Donnelly, C. Hassler, *et al.*, "Estimation of WECC system inertia using observed frequency transients," *IEEE Transactions on Power Systems*, vol. 20, no. 2, pp. 1190–1192, 2005.

[13] P. M. Ashton, C. S. Saunders, G. A. Taylor, A. M. Carter, and M. E. Bradley, "Inertia estimation of the GB power system using synchrophasor measurements," *IEEE Transactions on Power Systems*, vol. 30, no. 2, pp. 701–709, 2014.

[14] D. Zografos, M. Ghandhari, and R. Eriksson, "Power system inertia estimation: Utilization of frequency and voltage response after a disturbance," *Electric Power Systems Research*, vol. 161, pp. 52–60, 2018.

[15] D. Zografos and M. Ghandhari, "Power system inertia estimation by approaching load power change after a disturbance," in *2017 IEEE Power & Energy Society General Meeting*, pp. 1–5, IEEE, 2017.

[16] J. Zhao, Y. Tang, and V. Terzija, "Robust online estimation of power system center of inertia frequency," *IEEE Transactions on Power Systems*, vol. 34, no. 1, pp. 821–825, 2018.

[17] T. Inoue, H. Taniguchi, Y. Ikeguchi, and K. Yoshida, "Estimation of power system inertia constant and capacity of spinning-reserve support generators using measured frequency transients," *IEEE Transactions on Power Systems*, vol. 12, no. 1, pp. 136–143, 1997.

[18] G. Rietveld, P. S. Wright, and A. J. Roscoe, "Requirements and test conditions for reliable rate-of-change-of-frequency measurements," in *2019 IEEE 10th International Workshop on Applied Measurements for Power Systems (AMPS)*, pp. 1–6, IEEE, 2019.

[19] K. Tuttelberg, J. Kilter, D. Wilson, and K. Uhlen, "Estimation of power system inertia from ambient wide area measurements," *IEEE Transactions on Power Systems*, vol. 33, no. 6, pp. 7249–7257, 2018.

[20] F. Zeng *et al.*, "Online estimation of power system inertia constant under normal operating conditions," *IEEE access*, pp. 101426–101436, 2020.

[21] Z. Jiang *et al.*, "Probing-Based Inertia Estimation Method Using Hybrid Power Plants," in *IEEE Power & Energy Society General Meeting (PESGM)*, pp. 1–5, IEEE, 2023.

[22] M. Rauniyar *et al.*, "Evaluation of probing signals for implementing moving horizon inertia estimation in microgrids," in *52nd North American Power Symposium*, pp. 1–6, IEEE, 2021.

[23] T. Lin, A. M. Gole, M. K. Das, G. D. Irwin, A. L. Issacs, and D. A. Woodford, "An online probing frequency injection method for Grid-Forming IBRs inertia measurement," *Cigre Science and Engineering*, vol. CSE N32, 2024.

[24] P. Kundur, *Power System Stability and Control*. New York: McGraw-Hill, 1994.

[25] 2010. Manitoba HVDC Research Centre, PSCAD/EMTDC Users guide, Winnipeg, Canada.

[26] A. Gole and V. Sood, "A static compensator model for use with electromagnetic transients simulation programs," *IEEE Transactions on Power Delivery*, vol. 5, no. 3, pp. 1398–1407, 1990.

[27] A. D. Paquette and D. M. Divan, "Virtual Impedance Current Limiting for Inverters in Microgrids With Synchronous Generators," in *IEEE Transactions on Industry Applications*, pp. 1630–1638, 2015.

[28] S. P. Me, S. Zabihi, F. Blaabjerg, and B. Bahrani, "Adaptive virtual resistance for postfault oscillation damping in grid-forming inverters," *IEEE Transactions on Power Electronics*, vol. 37, no. 4, pp. 3813–3824, 2021.